nature nanotechnology



Article

https://doi.org/10.1038/s41565-025-02005-z

Electrically driven heterostructured far-infrared wire lasers with integrated graphene plasmons

Received: 24 February 2025

Accepted: 4 August 2025

Published online: 30 October 2025

Check for updates

Alessandra Di Gaspare¹, Sara Ghayeb-Zamharir¹, Lianhe Li ©², Edmund H. Linfield **1**², Alexander G. Davies **1**², Jincan Zhang **1**³, Osman Balci³, Andrea C. Ferrari³ & Miriam S. Vitiello © 1 🖂

Photonic technologies that exploit surface plasmons in graphene can offer groundbreaking opportunities for the development of compact and inexpensive active photonic devices, owing to the unique combination of tight field localization, giant optical nonlinearities and electrostatic gating tuning. Here we take advantage of this unique combination of properties to engineer frequency up-converted, electrically driven, single-mode photonic sources in the 9.0–10.5 THz range, with an emission frequency entirely tunable by design. We excite plasmons confined in a multilayer graphene micro-ribbon grating within a distributed-feedback terahertz quantum cascade laser that incorporates a top supercapacitor to tune the graphene Fermi energy, demonstrating third harmonic generation. Our monolithic, electrically driven laser works in the inaccessible Reststrahlen band of its core III-V semiconductor heterostructure and shows a peak power of ~9 µW, laying the foundation of a new generation of plasmonic, nonlinear light-emitting sources.

Collective charge excitations (plasmons) in single-layer graphene (SLG)^{1,2} present strong similarities to the electromagnetic waves that propagate at the interface between a metal and a dielectric (surface plasmons)³. Specifically, they are characterized by a transversemagnetic polarization⁴ and by an exponentially decaying electric field amplitude in the direction orthogonal to the SLG plane⁵. However, owing to the Dirac-like band profile and locked in-plane electron motion, SLG plasmons have distinctive features that differentiate them from metal surface plasmons⁶, including a tighter field localization and reduced propagation losses^{1,2,4,5}. Importantly, the SLG plasmon charge can not only be electrostatically controlled through doping but also by gating^{7,8}, so that the behaviour of SLG surface plasmon-based structures can be modified in situ without the need for structural device modifications. At terahertz (THz) frequencies, this can be combined with the graphene's tunable optical properties^{8,9}, offering groundbreaking opportunities for creating compact electrically controllable THz optical components¹⁰; reconfigurable metamaterials¹¹⁻¹³; robust, fast (hundred picoseconds response times), cheap and scalable THz frequency photodetectors^{13–15}; and novel light sources^{16–18}. However, at THz frequencies, electromagnetic radiation cannot couple directly into bidimensional plasmon excitations and so structures engineered on a subwavelength scale are required, up to 200 times smaller than the wavelength in vacuum¹⁹—the simplest geometry being a periodic grating of graphene micro-ribbons^{20,21}. In this case, the plasmon resonance energy scales as $n^{1/4}$ (*n* being the carrier density) for Dirac plasmons in a micro-ribbon array, and as w^{-2} (w being the ribbon width). The combination of electrical and optical tuning thereby allows the properties of the graphene plasmons to be tailored.

Plasmonic effects can be used to confine THz fields to a subwavelength volume, exploiting the high degree of spatial confinement of graphene plasmons. They can also be used for efficient

NEST, CNR-NANO and Scuola Normale Superiore, Pisa, Italy. 2School of Electronic and Electrical Engineering, University of Leeds, Leeds, UK. 3Cambridge Graphene Centre, University of Cambridge, Cambridge, UK. Me-mail: miriam.vitiello@sns.it

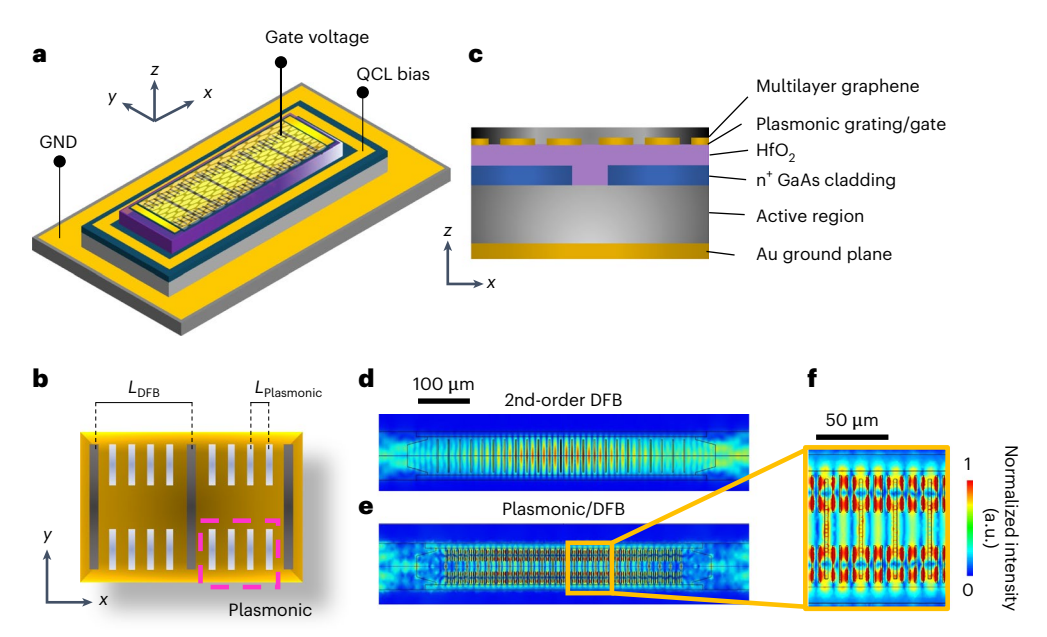


Fig. 1| **Device concept. a–c**, Schematic perspective view of the hybrid plasmonic QCL design (a), featuring a surface-emitting, 2nd-order DFB grating fabricated within the top contact of a double-metal waveguide resonator, with emission centred at -3.3 THz ($L_{\rm DFB}$ = 25.5 μ m). The ground (GND) is the bottom part of the QCL double-metal waveguide. The gate voltage is applied on the top. **b**, An overlapping plasmonic MLG/Au ribbon array (pink dashed region in **b**, $L_{\rm Plasmonic}$ = 5.1 μ m) enhances the intracavity field of the fundamental lasing mode of the DFB cavity. The cross-sectional view of the design (**c**) illustrates the layer sequence. A 30-nm-thick dielectric layer of HfO₂ between the top contact and the plasmonic/DFB metal contact (purple region in **c**) allows tuning of the Fermi

energy $E_{\rm F}$ through the field effect, and hence active control of the MLG optical conductivity, and the resulting field coupling and confinement. The dashed box in **b** marks the top view of the section shown in **c**. **d**–**f**, Electric field distribution of the graphene-integrated QCL cavity simulated using a 3D eigenfrequency study in COMSOL Multiphysics for the standard surface-emitting DFB (that is without plasmonic grating) at the fundamental eigenmode at 3.226 THz (**d**) and including the plasmonic/DFB grating at 3.220 THz (**e**,**f**). Panel **f** shows a magnified area of the plasmonic grating, highlighting the field enhancement in the graphene ribbons at the fundamental TM₀₀ mode. a.u., arbitrary units.

up-conversion in graphene—also known as harmonic generation (HG). Indeed, the giant SLG nonlinearities ($\chi^{(3)} \approx 10^{-9} \text{ m}^2 \text{ V}^{-2}$)²², observed in the far-infrared, governed by graphene's intraband carrier dynamics²³, combined with the inherent ultrafast (picoseconds) carrier dynamics, have enabled high HG at THz frequencies using only moderate fields and at room temperature²⁴.

Here we exploit the tight field localization and the giant optical nonlinearities of graphene plasmons to engineer frequency up-converted electrically pumped photonic sources across the 6.0–12.5 THz (24–50 μm wavelength) range. This overcomes the current lack of a spectrally narrowband solid-state-based technology that can access the whole 6.5–12.0 THz frequency range.

Results and discussion

Device engineering

For our benchmark device, we engineer a surface-emitting distributedfeedback (DFB)²⁵ double-metal²⁶ quantum cascade laser (QCL)a semiconductor heterostructure laser relying on intersubband transitions²⁷⁻²⁹—to include a superimposed multilayer graphene (MLG) plasmonic grating (a graphene ribbon array) and a top capacitor (acting as a gate electrode) (Fig. 1a-c). The DFB resonator is designed with a slit periodicity tuned to match the centre of the gain bandwidth (3.25–3.35 THz) of the selected QCL active region^{30,31}; the DFB grating is intended to govern the desired photonic momentum and the frequency of the mode propagating along the longitudinal direction of the resonator bar. The intracavity integrated plasmonic ribbon grating then provides the field enhancement needed for HG, while the top capacitor enables efficient tuning of the graphene Fermi level by electrostatic gating. The result is a double-grating resonator integrated into the top contact of a THz QCL incorporating a second-order DFB grating³², for the optimal control of the mode within the laser optical band, overlapping a plasmonic grating, which

induces a strong local electric field enhancement needed to drive frequency up-conversion.

We first numerically simulate the resonator to identify the optimal double-grating design. The double-metal waveguide QCL was modelled using COMSOL Multiphysics, with a finite element method solver (Supplementary Section 1). The plasmonic/DFB design was optimized by initially conducting a parametric study on the double-grating resonator unit cell (Supplementary Section 1). This was followed by three-dimensional (3D) simulations of the complete laser structure (Fig. 1a-c), which includes top Cr side absorbers to suppress the lateral cavity modes³³. Initially, we compared two structures: (i) a standard MLG-coated DFB structure (without the plasmonic grating; Fig. 1d) and (ii) the combined plasmonic/DFB grating device of Fig. 1a-c (Fig. 1e).

The 3D model of the MLG-coated DFB structure shows a fundamental eigenmode at frequency $v_{DEB} \approx 3.226$ THz (quality factor $Q_{\rm DFB} \approx 71$) (Fig. 1d), demonstrating that the integration of the MLG in the slits neither affects the resonator modes nor prevents laser action. The plasmonic grating is integrated into the top contact of the DFB resonator (Fig. 1a-c). To mitigate the induced increase in the total losses, we only patterned the MLG ribbon array towards the edges of the top contact region, that is, leaving the central region untouched (Fig. 1b). The MLG plasmonic grating leads to an eigenmode at $v_{\rm pl} \approx 3.220 \, \text{THz}$ (Fig. 1e,f), with a field distribution resembling that of the fundamental mode, aside from a slightly different field lobe distribution along the y axis. Importantly, we observe a substantial optical coupling inside the plasmonic slits between the intracavity field and the MLG (Fig. 1f). The *Q* value of the fundamental eigenmode v_{fi} , $Q_{fi} \approx 29$, is lower than that of the MLG-coated DFB, as a consequence of the increased optical losses introduced by the plasmonic slits. However, the electric field amplitude in the MLG is amplified, on average, by a factor $A_{ave} \approx 2.5$. This value is obtained by calculating the average electric field amplitude across the entire top contact surface. In the central region of the

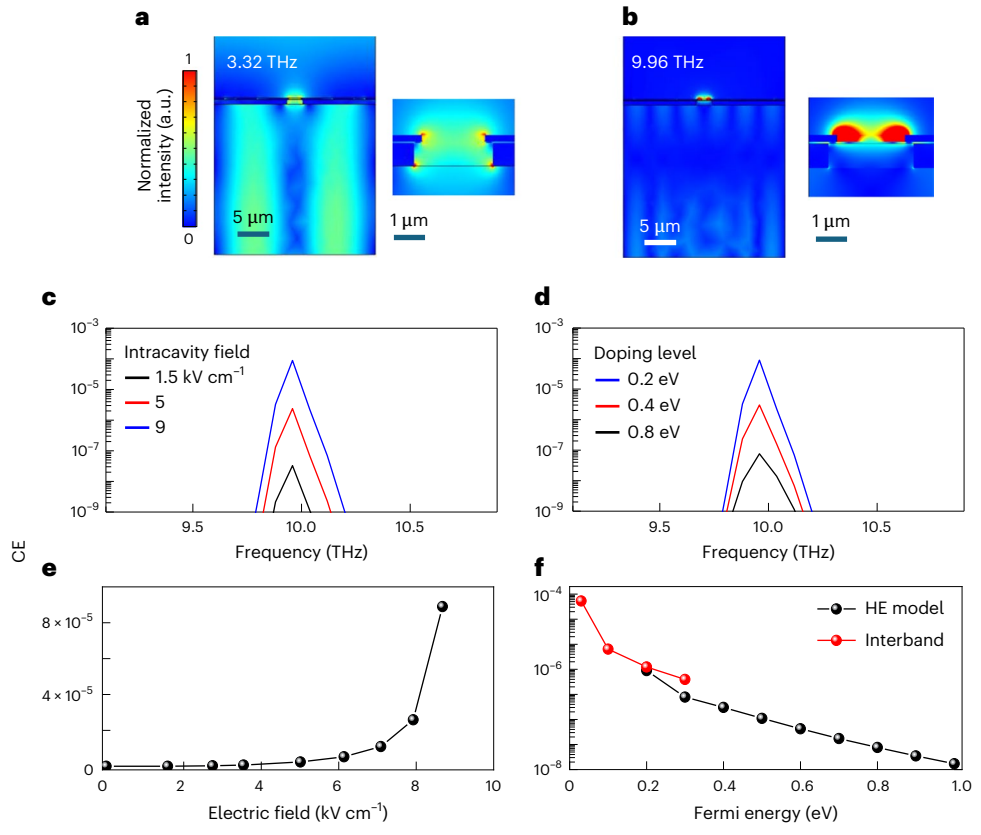


Fig. 2 | Simulation of the on-chip frequency up-conversion process. a,b, Cross-sectional views of the surface electric field distribution calculated at the fundamental mode at ~3.32 THz (a) and the third harmonic frequency of ~9.96 THz (b), for the DFB/plasmonic resonator coated with three layers of graphene, simulated by employing a surface current density numerical model to run two-dimensional simulations with the frequency domain module of COMSOL Multiphysics. The right sides of a and b show the magnified views of the electric field in the DFB slit region, respectively; the intensity of the colour map in b is a ×300 magnification of the intensity of that in a. The length of the unit cell along the x axis matches the periodicity of the DFB array (25.5 μm). The GaAs active region was modelled as a constant refractive index material in the THz range (n = 3.6), with the DFB grating realized by etching an air hole of 0.7 μ m depth and 2.5 µm width inside the doped layer. The refractive index of HfO2, as a gate dielectric with 30 nm thickness, was set at 4.24. An array of slits with periodicity 1/5 of the DFB periodicity were incorporated into the metal and then coated with $three \, layers \, of \, graphene, thus \, realizing \, graphene \, micro-ribbons \, embedded \, in \,$

the top metal, here modelled as a perfect electric conductor. Perfectly matched layer and perfect electric conductor boundary conditions were selected for the top and bottom directions along z (see Fig. 1c), respectively, while periodic boundary conditions were set along x (see Fig. 1c). All the simulations were performed using a single periodic excitation port, illuminating the top surface. To mimic the intracavity field intensity driving the nonlinear response in the plasmonic array, the input port power was set to 300 mW, concentrated over the area of a single DFB slit. c,d, TH CE as a function of frequency for different intracavity fields (c) and values of $E_{\rm F}(\mathbf{d})$. Other graphene parameters were electron mobility 1,400 cm² V⁻¹ s⁻¹ and scattering time 23 fs. e, CE as a function of the intracavity electric field, assuming $E_F = 200$ meV. **f**, CE as a function of E_F, assuming an intracavity field of ~8.6 kV cm⁻¹, calculated using a 3rd-order nonlinear model based on hot electron (HE) intraband absorptions (black) at $E_{\rm F} \ge 200$ meV, and interband multiphoton absorptions (red) at $E_{\rm F} \le 200$ meV, respectively. $E_{\rm F}$ is assumed equal to 200 meV in ${\bf a}-{\bf c}$ and ${\bf e}$; the intracavity field is assumed equal to ~8.6 kV cm⁻¹ in **f**. a.u., arbitrary units.

plasmonic grating, where the enhancement of the intracavity field is maximum, the amplification is increased by almost 2 orders of magnitude, $A_{\text{peak}} \approx 10^2$.

Simulation model of the frequency up-conversion process

To evaluate the role of the electric field enhancement on the HG process occurring in the top surface grating (MLG ribbons), and to estimate the expected HG conversion efficiency (CE), we follow the approach of ref. 34. This method allows the third harmonic generation (THG) efficiency to be extracted as an output parameter directly from the simulations, by setting up the equations for the third harmonic generated field in the software module. The method assumes that the MLG is a nonlinear surface current generator (Supplementary Section 2) and computes the CE (Supplementary Sections 3 and 4) of the THG process by solving the Maxwell equations at the third harmonic frequency, assuming a quasi-continuous wave excitation with an average 300 mW input power.

The calculated surface electric field distribution at the fundamental mode -3.32 THz (Fig. 2a) and at the TH frequency -9.96 THz

(Fig. 2b) for the double-grating QCL with a 3-layer graphene plasmonic ribbon grating shows that, at the TH frequency (Fig. 2b), the field distribution mimics that retrieved at the fundamental mode, with a field intensity more than 2 orders of magnitude lower. Figure 2c,d shows the calculated CE as a function of frequency, at different intracavity fields and MLG Fermi energies, $E_{\rm F}$, respectively. At three times the fundamental frequency, the predicted CE is -10⁻⁴ for a moderate value of $E_{\rm F}$ -200 meV. The calculated decrease in the TH peak intensities for increasing $E_{\rm F}$ (Fig. 2f) differs from previous reports³⁵ on TH CEs in doped graphene, where the nonlinear response is stronger in highly conductive Dirac systems³⁵. This behaviour stems from the different excitation dynamics provided by the quasi-continuous wave laser, adopted in the present case.

At the Dirac point, a larger CE is predicted to be achieved (Fig. 2f). However, the very low Fermi energies (<50 meV) required to achieve this condition are extremely difficult to realize in large-area graphene, even with a very efficient gate tuning. A more reliable comparison is then with the CE calculated at the Fermi level $E_{\rm F} \approx 200$, that is, the value set after optimizing our simulations. We set the

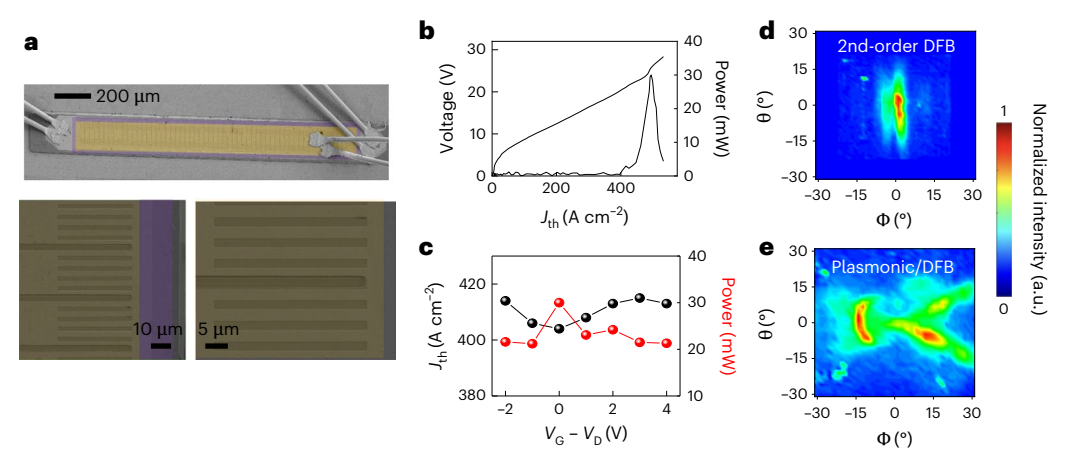


Fig. 3 | **Device fabrication, electrical and optical characterization. a**, Scanning electron microscope images of a prototypical fabricated device, showing the top DFB/plasmonic grating (yellow, false colour) and the gate oxide area (purple). The grating comprises a plasmonic ribbon of width $W_{\rm pl} \approx 2~\mu{\rm m}$ and a ribbon spacing of 1/5 of the periodicity of the DFB array. At such a ribbon width, the plasmonic resonance of the MLG/Au ribbon grating, on the lateral edges of the top metal, matches the DFB mode. **b**, Light-current density-voltage (L-J-V) characteristics measured on a 1.5 × 0.2 mm-sized plasmonic/DFB QCL bar, when driving the QCL in pulsed mode with a pulse width of 1 $\mu{\rm s}$ (duty cycle 5%) at 15 K.

c, QCL threshold current density (left axis, black) and emission power (right axis, red), as a function of the gate voltage. **d,e**, Far-field profiles measured for a standard DFB (**d**) and a plasmonic/DFB (**e**) QCL, realized on the same active region and with the same DFB array geometry. The far-field profiles were measured under the same conditions of **b**, at a driving current corresponding to the peak optical power, while raster scanning a pyroelectric detector placed at -5 cm from the laser surface, in the plane parallel to the laser surface, and projecting the two-dimensional signal onto a spherical surface, identified by the azimuthal (Φ) and the polar (θ) angles. a.u., arbitrary units.

maximum intracavity power at $0.3 \, \text{W}$ ($\approx 9 \, \text{kV}$ cm⁻¹ intracavity field) (Fig. 2e) in our analysis, because our model loses validity at higher powers as the electronic temperature becomes higher than the Fermi temperature. Under the latter conditions, the smearing-out of the carrier distribution opens a channel for interband transitions³⁶, involving multiphoton absorption³⁷ beyond Pauli blocking, that must be taken into account when evaluating the CE (Fig. 2f). It is worth mentioning that at $3\nu_0$, Reststrahlen band phonons play no role in the TH up-conversion process, since, in our geometry, the nonlinear effects inducing THG take place in a very confined volume ($<0.1 \, \mu \text{m}^3$) around the plasmonic ribbon surface, and so they are spatially separated by the absorbing medium (Supplementary Section 4).

Demonstration of efficient THG

We then fabricate a set of surface-emitting double-metal QCLs following the device schematics in Fig. 1a–c, using a high-power THz QCL delivering 2.5 W peak power 30,31 (Supplementary Sections 5 and 6). The DFB grating (Fig. 3a) was designed as a linear array of 2.5- μ m-wide, 800-nm-deep slits in the top metal/doped layer. After patterning the top DFB grating, using optical lithography, followed by the removal of the doped GaAs from the slits, we cover the top cladding layer with an -30-nm-thick layer of HfO₂ using atomic layer deposition. This enables field-effect gate coupling of the MLG in the top emitting surface and the electronic control of E_F . We then used electron beam lithography to pattern the top plasmonic grating by aligning the DFB/plasmonic grating pattern with the underlying DFB slits. The MLG transfer was performed by a poly(methyl methacrylate) (PMMA)-assisted wet method 38 , using sequential SLG transfers (Methods and Supplementary Section 7), placing three graphene layers on the QCL devices.

We fabricated seven devices, each demonstrating a consistent behaviour (Supplementary Section 8). The voltage–current density–light characteristic (Fig. 3b for one typical device) shows a maximum peak optical power of -30 mW. The presence of the static gate electrode coupled with the laser top contact (Fig. 3a) has only a marginal impact on both the emitted optical power and laser threshold, with the latter varying by \leq 10 A cm⁻² at the highest gate voltage (Fig. 3c). However, the gate bias (V_G) provides an efficient tool to change the MLG E_F , and enables tuning of the CE, as predicted by the theoretical model (Fig. 2d,f). The comparison between the far-field intensity profile of the integrated

laser (Fig. 3e) and that of a standard surface-emitting 2nd-order DFB QCL (Fig. 3d and Supplementary Section 9) shows that, while the typical single lobe profile with $\sim 10^{\circ}$ divergence is obtained in the latter case, the plasmonic grating induces two side lobes with an -15° angular broadening. This is understood by considering the field coupling of the two series of plasmonic slits, defined along the two edges of the top contact. Raman spectroscopy was used to confirm the MLG quality following transfer on the QCL device⁴⁰ (Supplementary Section 7).

To verify the occurrence of the expected third-order frequency up-conversion process, we mounted the devices in a Fourier transform infrared (FTIR) spectrometer under vacuum and collected spectra in step-scan mode over long acquisition times. To isolate the third harmonic terms at $3\nu_0$ from the fundamental 2nd-order DFB lasing mode at ν_0 , we used a high-pass thallium filter (Crystan) positioned in front of a Si-bolometer detector. This suppresses >95% of the power <6 THz (ref. 41), with a transmittance \geq 50% in the 6-7 THz range, and \geq 70% at frequencies >8 THz (Supplementary Section 10).

Figure 4a-f plots the rapid-scan unfiltered (Fig. 4a-c) spectra, and step-scan filtered (Fig. 4d-f) emission spectra, at different gate voltages, measured on three devices. The first two devices of Fig. 4a,b were fabricated with a 2nd-order DFB pitch slightly detuned in frequency, within the 0.5-GHz-wide bandwidth of the QCL (Supplementary Section 6). The third device (Fig. 4c) belongs to a different fabrication batch, realized with an improved fabrication process, in which the DFB slits have been dry etched to engineer smoother sidewalls and a flat surface, preventing possible under-etching effects. At zero V_{G} , the measured v_0 is in agreement with the DFB grating design, in which photons are backscattered if the condition $k_p = 2k_B - k_p$ is fulfilled, with $k_{\rm B}$ and $k_{\rm p}$ being the wavevector of the Bragg peak and of the photon in the waveguide, respectively. v_0 consistently tunes with V_G , red-shifting by ~15 GHz V⁻¹ for the sample of Fig. 4a, and by ~5 GHz V⁻¹ for the sample of Fig. 4c, as V_G approaches the MLG minimum conductivity point. In our integrated structures, it occurs at $V_G = +5$ V, close to V_D , the Dirac voltage measured on an ideal MLG field-effect transistor (FET) with an identical gate architecture (Fig. 4g). A visible mode hop is noticeable in Fig. 4b, which is the cause of the different retrieved lineshapes and frequency shift. The observed trend is likely related to the refractive index variations (and corresponding emission frequency variations) owing to gain change with the pump current that can be estimated

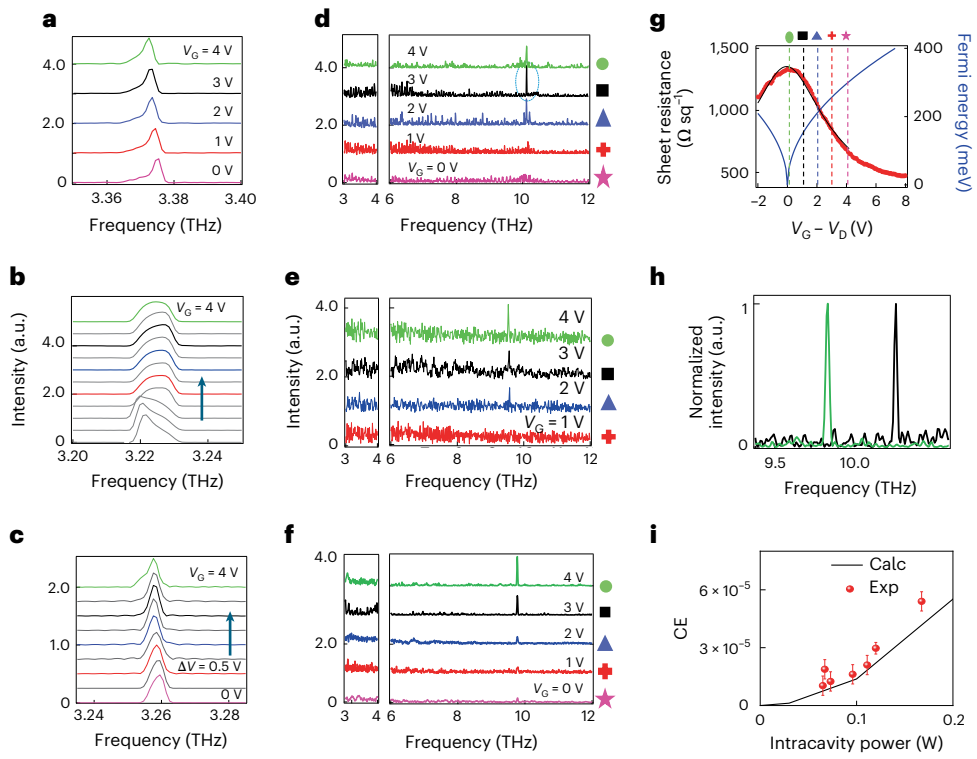


Fig. 4 | THG and CE. a-c, Stacked normalized FTIR emission spectra acquired, while driving the QCL with a current corresponding to the peak optical power, as a function of the gate voltage V_G , for three QCLs with differing DFB grating pitches $(\mathbf{a}-\mathbf{c})$, and fabricated with an optimized dry etching fabrication protocol (\mathbf{c}) . The spectra were measured in rapid-scan mode, under vacuum, using a helium-cooled Si bolometer (IRLabs), with a spectral resolution of 0.075 cm⁻¹. The QCL in **b** is initially emitting at 3.222 THz; this frequency initially red-shifts with tuning of the graphene Fermi level, but the QCL then mode hops at 3.228 THz before red-shifting up to 3.225 THz as V_G increases to 4 V. At zero gate bias (V_G), $v_0 = 3.375 \text{ THz}(\mathbf{a}), v_0 = 3.221 \text{ THz}(\mathbf{b}) \text{ and } v_0 = 3.262 \text{ THz}(\mathbf{c}). \mathbf{d} - \mathbf{f}, \text{ Stacked FTIR}$ emission spectra acquired in step-scan mode, under the same experimental conditions as a-c with a spectral resolution of 1 cm⁻¹, and filtering out the QCL lasing modes with a Ta high-pass filter (cut-off -7 THz), for the three QCLs in a (d), $\mathbf{b}(\mathbf{e})$ and $\mathbf{c}(\mathbf{f})$. The step-scan signal was retrieved with a lock-in amplifier (Stanford Instruments), synchronized with an amplitude-modulated signal of 317 Hz, which was used to modulate the pulsed bias driving the OCL. The left sides of **d-f** show the step-scan spectra measured in the range of emission of the DFB QCL. In $\mathbf{a} - \mathbf{c}$, the traces are acquired at intermediate (grey) and specific gate voltages: $V_G = +4 \text{ V (green)}, +3 \text{ V (black)}, +2 \text{ V (blue)}, +1 \text{ V (red)}$ and $0 \text{ V (pink, } \mathbf{a} \text{ and } \mathbf{c}),$

that are marked by symbols in $\mathbf{d} - \mathbf{f}$; in these samples, we assume that the minimum conductivity point is at $V_G = V_D \approx 4.5 \text{ V. } \mathbf{g}$, Sheet resistance modulation as a function of the gate voltage applied to an ideal, microscopic MLG graphene FET, realized with the same gate architecture used for the top-QCL supercapacitor (left axis, red dots) to tune $E_{\rm F}$ The black curve is the fit to the experimental data. The V_G dependence of E_F (blue line, right axis) is extracted from $E_F = \hbar v_F \sqrt{\pi n (V_G)}$. **h**, Expanded view of the third harmonic signal measured at $V_G = +3$ V on the laser of a, highlighting an S/N ratio of about 20 (black curve), and at $V_G = +4$ V on the optimized laser of **c**, highlighting an S/N ratio of about 60 (green curve). i, Comparison between the calculated CE (Calc, black line) and the CEs retrieved experimentally (Exp. red dots) across a set of seven devices, the last one (intracavity power 0.17 W) belonging to the new batch, each having different intracavity powers, displayed as a function of the corresponding intracavity power (Supplementary Section 8). Data are presented as mean values ± standard error of the mean (s.e.m.) bar, calculated following the relative error method, namely considering the s.e.m. of the signal amplitude of the third harmonic signal, as extracted from the interferogram trace, according to the method illustrated in Supplementary Section 8, and assigning a corresponding linearly proportional value to the CE error bar. a.u., arbitrary units.

via the linewidth enhancement factor⁴². The pump current is indeed affected by the conductivity of the material layer in the ribbon apertures¹⁸.

In all three cases (Fig. 4d-f), a well-defined peak emerges above the noise level at $3v_0$ = 10.1 THz (Fig. 4d), 9.66 THz (Fig. 4e) and 9.78 THz (Fig. 4f), with a signal-to-noise ratio ranging from S/N ≈ 5 to S/N ≈ 60 (Fig. 4h) for $V_G \gtrsim V_D - 2$ V to $V_G \approx V_D$. These peaks correspond to the expected THG process in the MLG plasmonic grating. At $V_G < V_D - 2$ V, the THG peak is still visible but consistently decreases in amplitude and then disappears below the noise level. The same behaviour was confirmed in most of the devices tested (Supplementary Section 8), and was unequivocally ascribed to the MLG since any possible frequency up-conversion process, activated by nonlinearities in the AR or in the HfO₂ dielectric layer, was excluded (Supplementary Sections 12 and 14).

Experimental tuning of the CE

To corroborate our observations, we measured the gate modulation on an ideal FET, fabricated by using the same dielectric layer grown on doped GaAs, with a microscopic (10 × 10 μ m²) MLG channel. The resistivity (red dots, Fig. 4g) is then fit with $R(V_G) = \mu e n_{\text{Tot}} (V_G)^{-1} = \left[\mu e \sqrt{n_0^2 + n^2(V_G)} \right]^{-1} = \left[\mu e \sqrt{n_0^2 + \left(\frac{C_{\text{EG}}}{e}\right)^2 (V_G - V_D)^2} \right]^{-1}$.

From the fit, we extract a mobility $\mu \approx 1,400 \text{ cm}^2 \text{ V}^{-1} \text{ s}^{-1}$, a capacitance $C_{\text{EG}} \approx 215 \text{ nF cm}^{-2}$, a residual carrier density $n_0 \approx 3.28 \times 10^{12} \text{ cm}^{-2}$ and $V_D \approx 4.4 \text{ V}$. The maximum sheet resistance, retrieved close to the charge neutrality point, was ~1.4 k Ω sq⁻¹, indicating a non-negligible background doping, which is not modulated by the gate voltage. The E_F dependence of V_G is extracted from $E_F = \hbar v_F \sqrt{\pi n} (V_G)$. We assume that the gate voltage range probed on the QCLs roughly corresponds to E_F ranging from 50 meV to a maximum $\Delta E_F \approx 300 \text{ meV}$ (Fig. 4g). This assumption is explained as follows. In the largearea $(1.2 \times 0.12 \text{ mm}^2) \text{ MLG FET}$ embedded in the QCL, it is difficult to reach the charge neutrality point (V_D) owing to an inhomogeneous

 $E_{\rm F}$ over the sample surface, which prevents carrier depletion at a single gate voltage. The more likely scenario is the achievement of a minimum conductivity point at $V_{\rm G}$ corresponding to a low $E_{\rm F}$ that we assume to be ~50 meV, as also confirmed by Raman spectroscopy (Supplementary Section 7).

Through the optimized fabrication procedure used for the device of Fig. 4c,f, we could noticeably improve the S/N ratio at the third harmonic frequency, as can be seen from Fig. 4h, showing a direct comparison between the most intense peak retrieved in Fig. 4d (black trace in Fig. 4h) and the best normalized peak collected in the optimized emitter (green curve in Fig. 4h). It is worth mentioning that while a visible peak at the third harmonic frequency is retrieved, the spectra in the frequency range around 6.5 THz, where a possible peak owing to second harmonic emission should appear, are noticeably flat (Supplementary Section 13).

We then estimated the experimental THG CE, by considering the amplitude ratio between the intensities of the frequency up-converted and incident (intracavity) light beams. The intensity of the THG signal is retrieved directly from the interferogram that encodes the signal measured by the lock-in amplifier during the step-scan acquisition, and with a Ta filter in place that removes any optical signal below 4 THz (cut-off frequency 7 THz; Supplementary Section 10). The incident (intracavity) light is extracted from the interferogram collected without the filter, and then normalized accounting for the device internal quantum efficiency $(60\%)^{43}$, assuming -50% light absorption through the MLG^{44,45}. The procedure is discussed in detail in Supplementary Section 11 and follows the procedures described in ref. 41.

The intracavity power of each device (horizontal axis Fig. 4i) was quantified by considering the actual optical output power, measured with a calibrated Thomas Keating thermal detector placed in front of the cryostat window (Fig. 3b), and then normalized by the internal quantum efficiency (60%) and MLG absorption losses (50%). For the entire set of fabricated samples, the CE values range from ~1 to 5.4 \times 10 $^{-5}$ (Fig. 4i), matching our simulations. Assuming those values, we obtain a maximum third harmonic peak power, that is, at 9–10 THz, of 9.0 μ W (average power of 450 nW).

We also validated this estimate of the emitted power at the third harmonic, following the procedure that we used in a previous work (Fig. 4b in ref. 41) for the QCL shown in Fig. 4a. In this case, we isolated the up-converted signal, positioning an 7 THz high-pass Ta filter along the optical path in front of the window of a Ge bolometer (QMC), and detected directly the signal emitted by the integrated laser with a lock-in amplifier, referenced to the same signal used to amplitude-modulate the QCL, driven at a current corresponding to the peak power. Considering the detector responsivity (3.5 kV W $^{-1}$), the lock-in signal gave an optical power output at the third harmonic of 210 nW average power (4.1 μ W peak power), slightly larger but comparable with the number retrieved from the procedure described above.

Conclusion

The demonstration of frequency up-conversion, using electrically controllable graphene plasmons integrated into a semiconductor heterostructure laser, opens up a breadth of new device possibilities, including the tailored design of solid-state sources for the, normally inaccessible, 6.5–12.0 THz frequency range. Far-infrared spectroscopy of a large number of rotational and roto-vibrational transitions of light molecules and free radicals can be easily measured with the achieved 400 nW of average power levels, as already shown at lower frequencies (3 THz) with only 100 nW of optical power frequencies (3 THz) with only 100 nW of optical power liquids, such as water in the far-intrared range, where strong absorptions are present, or mapping the intricacies of protein function in amino acids such as dipeptides and tripeptides, in a frequency range in which they show resonances 1.5 such applications have not been extensively investigated so far owing to the lack of appropriate sources,

but would offer new insights into low-frequency intermolecular motions. This could provide vital information on, for example, the complex interaction of water molecules with atmospheric gases⁴⁸, their role in meso-structures (proteins and charge groups) of biological organisms⁴⁹, and enable fast detection of complex amino acids⁵⁰. The developed sources could also be exploited in detectorless near-field scattering-type scanning near-field optical microscopy systems for quantum nanoscopy applications in the unexplored 24–50 µm range where many plasmonic, phononic and magnetic phenomena of contemporary interest occur⁵¹. Indeed, by using re-injection of the up-converted light back into the QCL cavity, through the plasmonic grating, the QCL itself can be used as a transducer to reconstruct the near-field maps at multiple frequencies, including the high up-converted THz frequencies.

Technological strategies to increase the output power are likely to lead to wider uptake of the technology. These include (i) engineering the DFB resonator to comprise hybrid dielectric/metal side absorbers to suppress undesired lateral higher-order modes³⁹; (ii) more advanced and refined cavity designs that can substantially enhance the CE, for example, adopting plasmonic designs that offer better field enhancement than simple ribbon geometries⁵²; and (iii) designing a plasmonic lattice decoupled from the top surface of the laser device, or engineering a resonant cavity at a quarter wavelength thickness to increase further the local electric field density. The latter would lead to minimal changes in the optical losses but result in at least a one order-of-magnitude increase in extraction efficiencies. Those improvements can potentially also open up opportunities for the quantum control of condensed matter systems and their application in quantum computing architectures^{53,54}.

Online content

Any methods, additional references, Nature Portfolio reporting summaries, source data, extended data, supplementary information, acknowledgements, peer review information; details of author contributions and competing interests; and statements of data and code availability are available at https://doi.org/10.1038/s41565-025-02005-z.

References

- Grigorenko, A. N., Polini, M. & Novoselov, K. S. Graphene plasmonics. Nat. Photon. 6, 749–758 (2012).
- Koppens, F. H. L., Chang, D. E. & García de Abajo, F. J. Graphene plasmonics: a platform for strong light-matter interactions. *Nano Lett.* 11, 3370–3377 (2011).
- Barnes, W. L., Dereux, A. & Ebbesen, T. W. Surface plasmon subwavelength optics. *Nature* 424, 824–830 (2003).
- Alonso-González, P. et al. Controlling graphene plasmons with resonant metal antennas and spatial conductivity patterns. Science 344, 1369–1373 (2014).
- Fei, Z. et al. Gate-tuning of graphene plasmons revealed by infrared nano-imaging. *Nature* 487, 82–85 (2012).
- Jablan, M., Buljan, H. & Soljačić, M. Plasmonics in graphene at infrared frequencies. *Phys. Rev. B* 80, 245435 (2009).
- Das, A. et al. Monitoring dopants by Raman scattering in an electrochemically top-gated graphene transistor. *Nat. Nanotechnol.* 3, 210–215 (2008).
- 8. Ju, L. et al. Graphene plasmonics for tunable terahertz metamaterials. *Nat. Nanotechnol.* **6**, 630–634 (2011).
- 9. Bonaccorso, F., Sun, Z., Hasan, T. & Ferrari, A. C. Graphene photonics and optoelectronics. *Nat. Photon.* **4**, 611–622 (2010).
- Wang, X., Cheng, Z., Xu, K., Tsang, H. K. & Xu, J.-B. High-responsivity graphene/silicon-heterostructure waveguide photodetectors. *Nat. Photon.* 7, 888–891 (2013).
- Degl'Innocenti, R., Kindness, S. J., Beere, H. E. & Ritchie, D. A. All-integrated terahertz modulators. *Nanophotonics* 7, 127–144 (2018).

- Arezoomandan, S., Condori Quispe, H. O., Ramey, N., Nieves, C. A. & Sensale-Rodriguez, B. Graphene-based reconfigurable terahertz plasmonics and metamaterials. *Carbon N. Y.* 112, 177–184 (2017).
- Tredicucci, A. & Vitiello, M. S. Device concepts for graphenebased terahertz photonics. *IEEE J. Sel. Top. Quantum Electron.* 20, 130–138 (2014).
- Koppens, F. H. L. et al. Photodetectors based on graphene, other two-dimensional materials and hybrid systems. *Nat. Nanotechnol.* 9, 780–793 (2014).
- Asgari, M. et al. Chip-scalable, room-temperature, zero-bias, graphene-based terahertz detectors with nanosecond response time. ACS Nano 15, 17966–17976 (2021).
- Riccardi, E. et al. Ultrashort pulse generation from a graphenecoupled passively mode-locked terahertz laser. Nat. Photon. 17, 607–614 (2023).
- 17. Riccardi, E. et al. Terahertz sources based on metrological-grade frequency combs. *Laser Photon. Rev.* 17, 2200412 (2023).
- Chakraborty, S. et al. Gain modulation by graphene plasmons in aperiodic lattice lasers. Science 351, 246–248 (2016).
- Ginley, T., Wang, Y., Wang, Z. & Law, S. Dirac plasmons and beyond: the past, present, and future of plasmonics in 3D topological insulators. MRS Commun. 8, 782–794 (2018).
- 20. Jadidi, M. M. et al. Tunable terahertz hybrid metal-graphene plasmons. *Nano Lett.* **15**, 7099–7104 (2015).
- Jadidi, M. M. et al. Nonlinear terahertz absorption of graphene plasmons. Nano Lett. 16, 2734–2738 (2016).
- Hafez, H. A., et al. Terahertz nonlinear optics of graphene: from saturable absorption to high-harmonics generation. *Adv. Opt. Mater.* 8, 1900771 (2020).
- 23. Mics, Z. et al. Thermodynamic picture of ultrafast charge transport in graphene. *Nat. Commun.* **6**, 7655 (2015).
- Hafez, H. A. et al. Extremely efficient terahertz high-harmonic generation in graphene by hot Dirac fermions. *Nature* 561, 507–511 (2018).
- Faist, J. et al. Distributed feedback quantum cascade lasers. Appl. Phys. Lett. 70, 2670–2672 (1997).
- Williams, B. S., Kumar, S., Callebaut, H., Hu, Q. & Reno, J. L. Terahertz quantum-cascade laser at λ≈100 μm using metal waveguide for mode confinement. Appl. Phys. Lett. 83, 2124–2126 (2003).
- 27. Vitiello, M. S. & Tredicucci, A. Physics and technology of terahertz quantum cascade lasers. *Adv. Phys. X* **6**, 1893809 (2021).
- Faist, J., et al. Quantum cascade laser. Science 264, 553–556 (1994).
- 29. Köhler, R. et al. Terahertz semiconductor-heterostructure laser. *Nature* **417**, 156–159 (2002).
- 30. Song, C. et al. High-power density, single plasmon, terahertz quantum cascade lasers via transverse mode control. *Appl. Phys. Lett.* **122**, 121108 (2023).
- 31. Li, L. et al. Terahertz quantum cascade lasers with >1 W output powers. *Electron. Lett.* **50**, 309–311 (2014).
- Fan, J. A. et al. Surface emitting terahertz quantum cascade laser with a double-metal waveguide. Opt. Express 14, 11672–11680 (2006).
- 33. Salemi, L. et al. One-dimensional, surface emitting, disordered terahertz lasers. *APL Photon.* **5**, 036102 (2020).
- Guo, T., Jin, B. & Argyropoulos, C. Hybrid graphene-plasmonic gratings to achieve enhanced nonlinear effects at terahertz frequencies. *Phys. Rev. Appl.* 11, 24050 (2019).
- Pogna, E. A. A., et al. Electrically tunable nonequilibrium optical response of graphene. ACS Nano 16, 3613–3624 (2022).
- 36. Kovalev, S. et al. Electrical tunability of terahertz nonlinearity in graphene. Sci. Adv. 7, eabf9809 (2023).

- Cheng, J. L., Vermeulen, N. & Sipe, J. E. Third order optical nonlinearity of graphene. New J. Phys. 16, 53014 (2014).
- 38. Bonaccorso, F. et al. Production and processing of graphene and 2d crystals. *Mater. Today* **15**, 564–589 (2012).
- 39. Mahler, L. et al. Quasi-periodic distributed feedback laser. *Nat. Photon.* **4**, 165–169 (2010).
- 40. Ferrari, A. C. et al. Raman spectrum of graphene and graphene layers. *Phys. Rev. Lett.* **97**, 187401 (2006).
- 41. Di Gaspare, A. et al. Compact terahertz harmonic generation in the Reststrahlenband using a graphene-embedded metallic split ring resonator array. *Nat. Commun.* **15**, 2312 (2024).
- 42. Consolino, L. et al. Spectral purity and tunability of terahertz quantum cascade laser sources based on intracavity difference-frequency generation. *Sci. Adv.* **3**, e1603317 (2025).
- 43. Vitiello, M. S. et al. Probing quantum efficiency by laser-induced hot-electron cooling. *Appl. Phys. Lett.* **94**, 21115 (2009).
- 44. Di Gaspare, A. et al. Self-induced mode-locking in electrically pumped far-infrared random lasers. *Adv. Sci.* **10**, 2206824 (2023).
- 45. Dawlaty, J. M. et al. Measurement of the optical absorption spectra of epitaxial graphene from terahertz to visible. *Appl. Phys. Lett.* **93**, 131905 (2008).
- Consolino, L., Bartalini, S. & De Natale, P. Terahertz frequency metrology for spectroscopic applications: a review. J. Infrared Millim. Terahertz Waves 38, 1289–1315 (2017).
- Feng, K., Streyer, W., Zhong, Y., Hoffman, A. J. & Wasserman,
 D. Photonic materials, structures and devices for Reststrahlen optics. Opt. Express 23, A1418–A1433 (2015).
- Tennyson, J. et al. A database of water transitions from experiment and theory (IUPAC Technical Report). Pure Appl. Chem. 86, 71–83 (2014).
- 49. Vatansever, F. & Hamblin, M. R. Far infrared radiation (FIR): its biological effects and medical applications. *Photonics Lasers Med.* **4**, 255–266 (2012).
- Wang, L. et al. Quantitative analysis of homocysteine in liquid by terahertz spectroscopy. *Biomed. Opt. Express* 11, 2570–2577 (2020).
- 51. Basov, D. N., Fogler, M. M. & García de Abajo, F. J. Polaritons in van der Waals materials. Science **354**, aag1992 (2016).
- Di Gaspare, A. Second and third harmonic generation in topological insulator-based van der Waals metamaterials. *Light Sci. Appl.* https://doi.org/10.1038/s41377-025-01847-5 (2025).
- 53. He, Y. et al. A two-qubit gate between phosphorus donor electrons in silicon. *Nature* **571**, 371–375 (2019).
- 54. Greenland, P. T. et al. Coherent control of Rydberg states in silicon. *Nature* **465**, 1057–1061 (2010).

Publisher's note Springer Nature remains neutral with regard to jurisdictional claims in published maps and institutional affiliations.

Open Access This article is licensed under a Creative Commons Attribution 4.0 International License, which permits use, sharing, adaptation, distribution and reproduction in any medium or format, as long as you give appropriate credit to the original author(s) and the source, provide a link to the Creative Commons licence, and indicate if changes were made. The images or other third party material in this article are included in the article's Creative Commons licence, unless indicated otherwise in a credit line to the material. If material is not included in the article's Creative Commons licence and your intended use is not permitted by statutory regulation or exceeds the permitted use, you will need to obtain permission directly from the copyright holder. To view a copy of this licence, visit https://creativecommons.org/licenses/by/4.0/.

© The Author(s) 2025

Methods

MLG preparation and integration onto the QCL chip

The large-area SLG was synthesized on a copper substrate using chemical vapour deposition (CVD)⁵⁵. The SLG on Cu (1 cm × 1 cm) was then coated with a 20-nm-thick layer of polymer (A4-950K PMMA polymer) and cured at 90 °C for 60 s. The graphene film from the bottom surface of the CVD sample was then removed using oxygen plasma reactive ion etching, and the sample immersed, floating and face-up, in a solution of 1 g of ammonium persulfate and 40 ml of deionized water to etch the copper substrate, and remove completely the Cu sacrificial substrate. Once the copper etching was complete, the PMMA-SLG film was transferred into a beaker of deionized water and then scooped up with a second copper-graphene CVD sample, to form a two-layer graphene stack. This sample was left to dry completely. The copper of the bilayer graphene was then etched with the same technique. This process was repeated sequentially until the desired MLG thickness was reached, in this case three layers. The multi-stack was then transferred onto the top of the laser chip, left to dry and finally soaked in acetone to clean the surface and remove the PMMA.

Reporting summary

Further information on research design is available in the Nature Portfolio Reporting Summary linked to this article.

Data availability

The data presented in this study are available on reasonable request from the corresponding author.

Code availability

The relevant computer codes supporting this study are available from the authors upon reasonable request.

References

55. Viti, L. et al. Scalable terahertz room temperature photoreceivers based on large-area hexagonal boron nitride and graphene heterostructures. *Adv. Opt. Mater.* **13**, 2402100 (2025).

Acknowledgements

We acknowledge funding from the European Union through the FET Open project EXTREME IR (944735), EPSRC (UK) programme grants 'TeraCom' (EP/W028921/1) and 'NAME' (EP/V001914/1), the Henry Royce Institute grant EP/P022464/1, EU Graphene Flagship, ERC grants Hetero2D and GIPT, EU grants Graph-X and CHARM, and EPSRC grants EP/K01711X/1, EP/K017144/1, EP/N010345/1, EP/L016087/1. EP/V000055/1 and EP/X015742/1.

Author contributions

M.S.V. conceived the concept, engineered the device and supervised the study. A.D. fabricated the samples, performed the experiments and set the analytical model. S.G.-Z. performed the simulations. A.D. and M.S.V. analysed and interpreted the data. L.L., E.H.L. and A.G.D. grew the QCL heterostructure. O.B., J.Z. and A.C.F. grew the large-area high-quality graphene. M.S.V. wrote the paper with the contribution of A.D.G. All authors contributed to the final version of the paper.

Competing interests

The authors declare no competing interests.

Additional information

Supplementary information The online version contains supplementary material available at https://doi.org/10.1038/s41565-025-02005-z.

Correspondence and requests for materials should be addressed to Miriam S. Vitiello.

Peer review information *Nature Nanotechnology* thanks Hua Li and the other, anonymous, reviewer(s) for their contribution to the peer review of this work.

Reprints and permissions information is available at www.nature.com/reprints.

	4		
natureresearch			Corresponding author(s): Miriam Serena Vitiello NNANO-25020739B
•			☐ Initial submission ☐ Revised version ☐ Final submission
La	asing Reporting Summary		
rep ma		ency and t	nat we publish. This form is intended for publication with all accepted papers transparency in reporting. Some list items might not apply to an individual sta availability policy, see Authors & Referees.
١	Experimental design		
Ρle	ease check: are the following details reported in th	he manu	script?
1.	Threshold		
	Plots of device output power versus pump power over a wide range of values indicating a clear threshold	Yes No	Emitted power VS input current of the electrically pumpud lasers
2.	Linewidth narrowing		
	Plots of spectral power density for the emission at pump powers below, around, and above the lasing threshold, indicating a clear linewidth narrowing at threshold	XYes	Figures 4 how the emission in the spectral ranges of interest collected with an FTIR spectrometer. This techninque does not allow to estimated the lasing linewidth.
	Resolution of the spectrometer used to make spectral measurements	Yes No	Caption of Fig.4 includes the details
3.	Coherent emission		
	Measurements of the coherence and/or polarization of the emission	Yes No	Lasing reported in a quantum cascade heterisctructure. Ineherent Coherent emission
4.	Beam spatial profile		
	Image and/or measurement of the spatial shape and profile of the emission, showing a well-defined beam above threshold	XYes	Shown in Figures 3d,e
5.	Operating conditions		
	Description of the laser and pumping conditions Continuous-wave, pulsed, temperature of operation	Yes No	All the details are given in manuscript, figure captions and supporting information
	Threshold values provided as density values (e.g. W cm-2 or J cm-2) taking into account the area of the device	Yes No	Included in Figure 3, and in the Supplementary Information
6.	Alternative explanations		
	Reasoning as to why alternative explanations have been ruled out as responsible for the emission characteristics e.g. amplified spontaneous, directional scattering; modification of fluorescence spectrum by the cavity	X Yes	Modelling and data to support frequency upconversion carafully reported
7.	Theoretical analysis		
	Theoretical analysis that ensures that the experimental values measured are realistic and reasonable e.g. laser threshold, linewidth, cavity gain-loss, efficiency	Yes No	Detailed modelling in the manuscript and Supporting Information file
8.	Statistics		
	Number of devices fabricated and tested	Yes No	Supporting Information sections dedicated to the statistical analysis of the various devices tested and the number is propertly reported.

▶ Further reading

lifetime (time to failure)

We also suggest that authors read the following literature, which describes the important principles and signatures of laser emission and discusses some of the common mistakes that can occur during laser characterization.

Yes A statistical analysis of the main figures of merit is reported in the Supporting Information

The presented devices are extremelvery stable. Hence the inherent device lifetime (years) is much longer than a set of repeated experimental campaigns

- 1. Samuel I.D.W., Namdas, E.B. & Turnbull, G.A. How to recognize lasing. Nat. Photon. 3, 546-549 (2009).
- 2. Siegmann, A.E. Lasers. (University Science Books, 1990)

Statistical analysis of the device performance and

- 3. Svelto, O. Principles of Lasers. 5th edn. (Springer 2010)
- 4. Blood, P. Quantum Confined Laser Devices: Optical Gain and Recombination in Semiconductors. (Oxford Univ. Press, 2015)

No

5. Koxlov, V.G. et al. Laser action in organic semiconductor waveguide and double-heterostructure devices. Nature 389, 362-364 (1997).